



Comprehensive thermal analysis of a high stability Cu–Zr–Al bulk metallic glass subjected to high-pressure torsion

Ádám Révész¹ · Talaye Arjmandabasi¹ · Erhard Schafner² · David J. Browne³ · Zsolt Kovács¹

Received: 14 June 2022 / Accepted: 5 December 2022 / Published online: 1 January 2023
© The Author(s) 2022

Abstract

Bulk metallic glass of $\text{Cu}_{38}\text{Zr}_{54}\text{Al}_8$ nominal composition was synthesized by copper mold casting into 6 mm diameter rods. Disks of the as-cast glass were subjected to severe plastic deformation by high-pressure torsion for different number of revolutions. The microstructure and the thermal behavior of the as-cast, isothermally annealed and deformed glass have been investigated by X-ray diffraction and differential scanning calorimetry, respectively. Continuous heating experiments revealed a two-stage devitrification event with excellent glass forming parameters, such as glass transition ($T_g = 671$ K), supercooled liquid region ($\Delta T_x = 80$ K), reduced glass transition ($T_r = 0.57$) and gamma parameter ($\gamma = 0.41$). Power law crystal growth during diffusion-controlled homogeneous nucleation was observed for isothermal annealings. Glassy state was preserved almost in the entire sample volume of the as-cast alloy during the high-pressure torsion process, corresponding to the extreme stability of the $\text{Cu}_{38}\text{Zr}_{54}\text{Al}_8$ alloy against deformation-induced devitrification. This is in accordance with the transition of the reversible specific heat from the glassy to supercooled liquid state measured by modulated calorimetry. It was also concluded that glassy structure is more ordered in the severely deformed state.

Keywords Bulk metallic glass · Cu–Zr glass · High pressure torsion · Devitrification · Modulated calorimetry

Introduction

Bulk metallic glasses (BMGs) have drawn increasing attention in the past few decades due to their special structure and outstanding mechanical properties, such as high tensile strength and hardness, large elastic strain, excellent corrosion resistance and high stored elastic energy [1–5]. However, the widespread application of BMGs as structural materials has been limited due to their low ductility, brittleness and expensive alloying components [6–9]. These disadvantages are directly determined by the unique atomic configuration of BMGs, i.e., they possess only short range atomic order and lack structural faults, such as dislocations and grain boundaries [10, 11].

Among the large variety of different BMG classes, CuZr-based metallic glasses have recently attracted a great attention, due to their unexpensive components, enhanced thermal stability, high glass forming ability (GFA) [12–14], excellent corrosion resistance [15] and some intrinsic plasticity [16, 17]. The GFA of the Cu–Zr binary system is so outstanding that it is possible to cast the alloy into a bulk glassy form in wide composition range [18, 19]. The GFA concentration range in the ternary Cu–Zr–Ti system can be predicted by the vacancy formation energy, mixing enthalpy and configurational entropy [20]. The short-term heat treatment below the glass transition (T_g) of a CuZr-based BMG yields an increase in the thermal stability and a significant drop of the relaxation enthalpy [21]. The improved GFA of a CuZrAl ternary BMGs is attributed to the suppression of the precipitation of Cu–Zr phase and the efficient dense packing of atoms. [22]. As was demonstrated, chemical interaction of Cu with Al in a Cu-rich Cu–Zr–Al BMG induces preferential oxidation of Zr over Al, coupled with a strong Cu enrichment adjacent to the oxide growth front which leads to a reduced GFA [23]. It was found that the thermal stability decreases when Ti is alloyed to the Cu–Zr binary system

✉ Ádám Révész
reveszadam@ludens.elte.hu

¹ Department of Materials Physics, Eötvös University, P.O.B. 32, 1518 Budapest, Hungary

² Physics of Nanostructured Materials, Faculty of Physics, University of Vienna, 1090 Vienna, Austria

³ School of Mechanical and Materials Engineering, University College Dublin, Belfield Dublin 4, Ireland

[24], while a slight composition adjustment can make a considerable contribution to higher GFA and thermal stability [25].

During tensile deformation of CuZr-based BMGs, poly-morphic nanocrystals nucleate from the amorphous matrix [26], which are responsible for macroscopically detectable plastic strain and work hardening [27]. The understanding of thermally activated martensitic transformation behaviors well below room temperature of CuZr-based BMG composites can provide the fabrication shape memory alloys [28]. It was shown recently that the elastic modulus and hardness of a CuZrAl BMG synthesized by selective laser melting can be significantly improved [29]. The compression deformation behaviors of the ZrCu-based BMG samples was found to be size-dependent, i.e., the smallest sample exhibits the highest yield strength and compressive plasticity due to the larger free volume [30].

Besides nanocrystallization, the ductility of BMGs can be increased by dispersing the macroscopic external strain among a large number of shear bands generated by severe plastic deformation (SPD) by surface constraint techniques [31–34]. Among the different SPD techniques, high-pressure torsion (HPT) has received a considerable attention due to its extremely high applied shear strain in a relatively large sample volume [35, 36]. Briefly, during HPT deformation, a disk-shaped specimen is inserted between two stainless steel anvils and subjected to simultaneous torsional straining and uniaxial loading [37]. The combination of HPT and isothermal heat treatment below T_g of a $\text{Cu}_{46}\text{Zr}_{46}\text{Al}_8$ BMG can significantly improve the thermomechanical stability of the alloy which can further be used to tailor new design routes for other BMG systems [38]. We have shown that the microstructural and morphological features and thermal behavior of CuZr-based metallic glasses subjected to HPT have been correlated with the calculated temperature evolution in the disk based on 3-dimensional heat-conduction model [39, 40]. The effect of the deformation parameters, i.e., the shear rate [41] and accumulated shear on the microstructural and thermal behaviors of Cu–Zr-based glasses were demonstrated in detail [42].

In the current study we present that severe plastic deformation induces structural changes in a $\text{Cu}_{38}\text{Zr}_{54}\text{Al}_8$ BMG subjected to HPT. We highlight the effect of different devitrification routes, such as continuous heating experiment, isothermal annealings and HPT-deformation on the microstructure and thermal stability. Differences between the intrinsic thermal properties of the as-cast glass and the severely deformed alloy is investigated by modulated calorimetry. Mechanical characteristics and plastic behavior on micron-scale of the as-cast and HPT-deformed BMG will be compared in a forthcoming paper.

Experimental

Sample preparation

A bulk metallic glass cylinder with $\text{Cu}_{38}\text{Zr}_{54}\text{Al}_8$ nominal composition and diameter 6 mm was cast by suction casting into a Cu-mold in an arc furnace from liquid state under protective Ar atmosphere. The original ingot was produced in the same furnace by arc melting the high-purity components (> 99.9) and then the master alloy was flipped and remelted several times. The negative mixing enthalpy between any two components ($\Delta H_{\text{mix}}(\text{Zr}, \text{Cu}) = -23 \text{ kJ mol}^{-1}$, $\Delta H_{\text{mix}}(\text{Zr}, \text{Al}) = -44 \text{ kJ mol}^{-1}$, $\Delta H_{\text{mix}}(\text{Al}, \text{Cu}) = -1 \text{ kJ mol}^{-1}$) [43] provides the formation of atomic short range order during undercooling, which can promote increased packing efficiency and retards long-range diffusion of the atoms [1].

For subsequent severe plastic deformation, the as-cast BMG rod was cut into slices with a height of 1 mm. Thereafter, these disks were subjected to HPT in air, under an applied pressure of 8 GPa at room temperature with an angular velocity of $\omega = 0.2$ revolution/min for $N = 0.2$, $N = 1$ and $N = 5$ whole turns. For comparison a disk without torsion ($N = 0$) was also produced. In general, the accumulated shear strain (ϵ) for torsion deformation at a radius r can be given by

$$\epsilon = \frac{\theta r}{L} = \frac{2\pi N r}{L}, \quad (1)$$

where L and θ are the thickness of the disk and the rotation angle, respectively [37]. In the applied experimental HPT-setup the stainless steel anvils exhibited a constrained geometry [37].

Microstructural characterization

The structure of the as-cast BMG and deformed disks was examined by X-ray powder diffraction. The measurements were carried out on a Rigaku SmartLab diffractometer using Cu–K α radiation in $\theta - 2\theta$ geometry. The data were collected from 25 to 90° with a step size of 0.01°.

Thermal characterization

A Perkin Elmer power compensated differential scanning calorimeter (DSC) was used to investigate the thermal stability and crystallization behavior of the as-cast Cu–Zr–Al BMG rod and the deformed HPT-disk in a linear heating ramp performed at scan rates 5, 10, 20, 40 and 80 K min $^{-1}$. The corresponding ΔH_i transformation enthalpy values were obtained as the area of the exothermic peaks. Isothermal annealing treatments were also carried out by heating

the samples to T_{iso} temperatures at which the data were recorded for certain t_{iso} times. All measurements were carried out under protective Ar atmosphere. The temperature and the enthalpy were calibrated by using pure In and Al. The high temperature melting behavior of the as-cast BMG was examined by a Setaram Differential Thermal Analyzer (DTA) at heating rate of 10 K min^{-1} .

Modulated differential scanning calorimetry (MDSC) measurements were carried out by using a linear heating ramp modulated by a sinusoidal temperature program $T(t) = \beta \cdot t + \Delta T \cdot \sin(2\pi f \cdot t)$, where $\Delta T = 1 \text{ K}$ and $f = 0.01 \text{ Hz}$ are the amplitude and frequency of the modulation, respectively and $\beta = 1 \text{ K min}^{-1}$ is the applied constant average heating rate.

Results and discussion

Linear heating experiments

The XRD pattern of the as-cast $\text{Cu}_{38}\text{Zr}_{54}\text{Al}_8$ BMG ($d = 6 \text{ mm}$) is dominated by a broad halo ($2\theta \sim 37^\circ$) which undoubtedly confirms that the material is X-ray amorphous (see Fig. 1a), similarly to a $\text{Cu}_{44}\text{Zr}_{47}\text{Al}_9$ composition ($d = 4 \text{ mm}$) [44]. The corresponding linear heating DSC curve exhibits typical features of a glass, including the glass transition ($T_g = 671 \text{ K}$) followed by a two-stage crystallization sequence characterized by $T_{x1} = 759 \text{ K}$ and $T_{x2} = 860 \text{ K}$ transformation temperatures (see Fig. 1b), similar to the values obtained for other Cu–Zr-type BMGs. [39, 45, 46]. The width of supercooled liquid region $\Delta T_x = 80 \text{ K}$ ($\Delta T_x = T_{x1, \text{onset}} - T_g$) of the glass

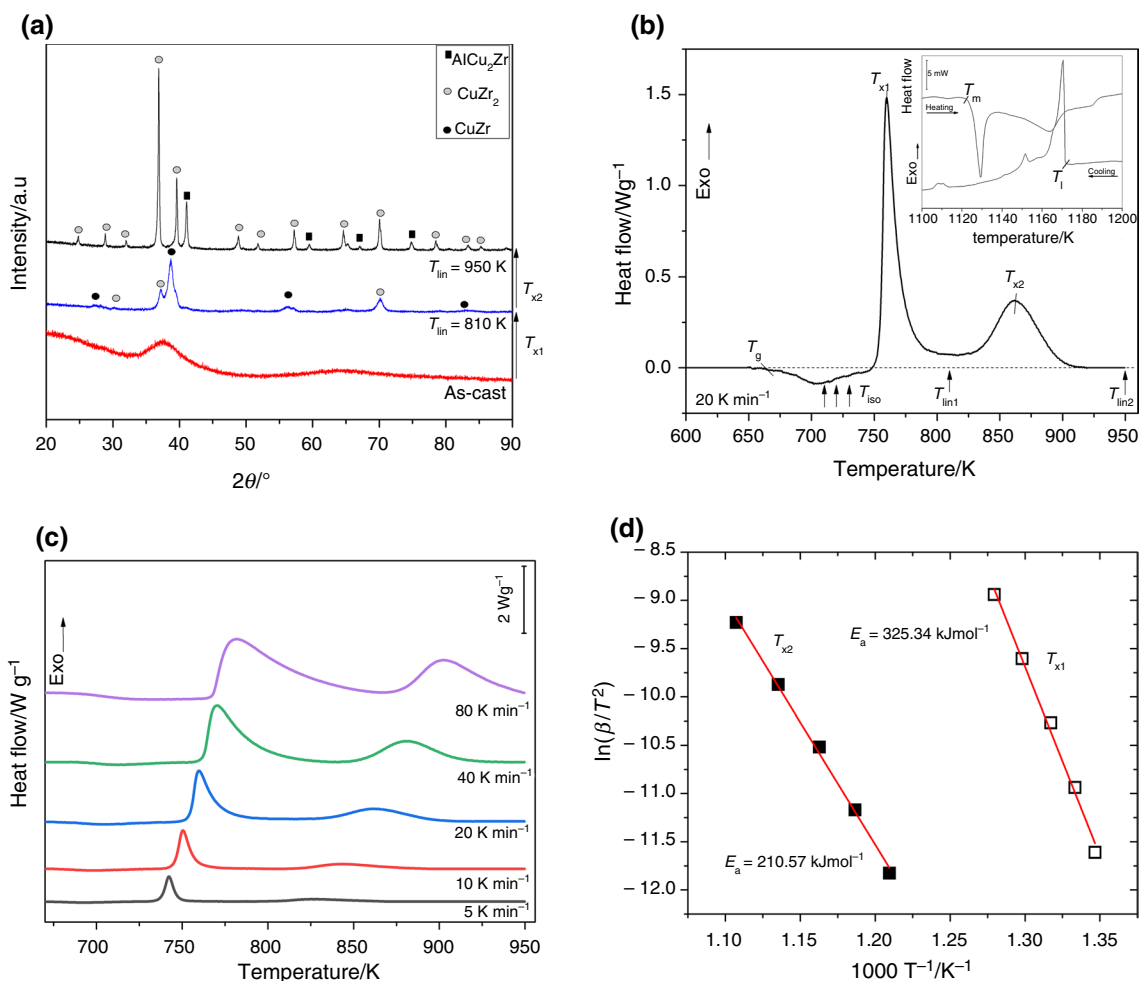


Fig. 1 **a** X-ray diffraction patterns of as-cast $\text{Cu}_{38}\text{Zr}_{54}\text{Al}_8$ metallic glass and states achieved by continuous heating. **b** Continuous-heating DSC curve of the as-cast BMG obtained at 20 K min^{-1} . The inset shows the melting and solidification of the alloy. **c** Continuous heat-

ing DSC curves obtained at different heating rates. **d** Kissinger plots obtained from the shift of the T_{x1} and T_{x2} transformation peak temperatures as a function of heating rate

corresponds to an extremely high GFA, slightly higher than was obtained for $\text{Cu}_{50}\text{Zr}_{43}\text{Al}_7$ BMG [47]. The extreme high value of ΔT_x may indicate that the undercooled liquid has a very strong resistance against crystallization either by thermal activation or by plastic deformation and therefore any primary nanocrystallization is retarded. The obtained values corresponding to the exothermal heat release ($\Delta H_1 = 67 \text{ Jg}^{-1}$ and $\Delta H_2 = 50 \text{ Jg}^{-1}$) are practically independent of the heating rate. As obtained from the inset of Fig. 1b, the liquidus temperature (T_l) determined from the high temperature DTA curve is 1173 K. Since the $\text{Cu}_{38}\text{Zr}_{54}\text{Al}_8$ composition is off-eutectic, the melting endotherms and the freezing exotherms turns into a multi-step process. To further investigate the GFA of the $\text{Cu}_{38}\text{Zr}_{54}\text{Al}_8$ composition, additional parameters have also been determined. The calculated reduced glass transition temperature $T_r = T_g/T_l$ (0.57) also indicates that the $\text{Cu}_{38}\text{Zr}_{54}\text{Al}_8$ system is an excellent glass former, similarly to other CuZr-based systems [46]. A much better interrelationship with the GFA incorporating both amorphization and devitrification processes has been introduced by Lu and Liu [48]. Accordingly, the $\gamma = T_x/(T_g + T_l)$ parameter calculated for the $\text{Cu}_{38}\text{Zr}_{54}\text{Al}_8$ glass ($\gamma = 0.41$) also confirms outstanding GFA.

Evolution of the microstructure during the crystallization sequence can be inferred from the corresponding XRD patterns (Fig. 1a). As one can notice, linear heating above the first crystallization event ($T_{\text{lin}1} = 810 \text{ K}$) results in a complete disappearance of the amorphous background, on the other hand the pattern is dominated by hexagonal CuZr (JCPDS 01-071-7931, $a = 0.5035 \text{ nm}$, $c = 0.3142 \text{ nm}$) and some traces of tetragonal CuZr_2 (JCPDS 01-071-7932, 0.32204 nm , $c = 1.11832 \text{ nm}$) can also be observed. The corresponding average crystallite size determined from X-ray line broadening [49] was found to be $10 \pm 1 \text{ nm}$ and $15 \pm 2 \text{ nm}$ for the CuZr and CuZr_2 phases, respectively. Continuous heating above the second exothermic transformation ($T_{\text{lin}2} = 950 \text{ K}$) results in the nucleation of a multicomponent AlCu_2Zr phase (JCPDS 03-065-5905), accompanied with the grain coarsening of the existing CuZr_2 phase, as evidenced by the sharpening of the Bragg-peaks. The final crystallite size was obtained as $35 \pm 3 \text{ nm}$ and $39 \pm 3 \text{ nm}$ for the CuZr_2 and AlCu_2Zr phases, respectively. Such kind of polymorphic transformation is typical for other CuZr-based metallic glasses [13, 39, 41].

Figure 1c focuses on the variation of the T_{x1} and T_{x2} peak temperatures with the applied heating rate. As being thermally activated processes, the individual crystallization events are expected to shift to higher temperatures with increasing heating rate, as confirmed by Fig. 1c. Among several models, the Kissinger analysis is extensively used to determine the activation energy (E_a) of thermally activated processes [50]. As known, the dependence of the

transformation peak temperatures (T_i) on the heating rate can be given by the

$$\frac{\beta}{T_i^2} = \frac{Z_i R}{E_{a,i}} \exp\left(\frac{-E_{a,i}}{RT_i}\right), \quad (2)$$

Expression, where Z and R are the frequency factor and the gas constant, respectively [50]. Plotting $\ln(\beta/T_i^2)$ versus T_i^{-1} enables the determination of $E_{a,i}$ for each thermal event from the slope of the fitted straight line, see Fig. 1d. The obtained values ($E_{a,x1} = 325 \text{ kJ mol}^{-1}$, $E_{a,x2} = 210 \text{ kJ mol}^{-1}$) are significantly high, in accordance with literature data on Cu–Zr–Al glasses with slightly different composition [43]. These values confirm the high thermal stability of the glass and suggest that the crystallization takes place through a nucleation and growth process [51]. The frequency factor, which corresponds to the probability that an atom having energy E_a joins an existing nucleus, can be obtained from the intercept of the fitted line with the ordinate. For the $\text{Cu}_{38}\text{Zr}_{54}\text{Al}_8$ BMG alloy, $Z_{x1} = 3.05 \cdot 10^{19} \text{ s}^{-1}$, which means that, if a constant frequency is assumed, the total amount of crystallized material can reach $5.08 \cdot 10^{-5} \text{ mol}$ in the first second of the transformation.

Isothermal annealings and crystallization kinetics

Isothermal annealing treatments of the as-cast $\text{Cu}_{38}\text{Zr}_{54}\text{Al}_8$ glass were carried out to understand better the nucleation mechanism in detail. The isothermal DSC curves obtained at different T_{iso} annealing temperatures in the range of 710–730 K are presented in Fig. 2a. As marked by arrows in Fig. 1b, these T_{iso} temperatures are significantly lower than T_{x1} and found within the ΔT_x supercooled liquid range. As seen, each isotherm starts with an incubation period which is followed by a single exothermic peak. This shape of isotherms corresponds to a crystallization process that occurs through the formation of nuclei from the amorphous matrix followed by a growth mechanism [52]. This is in correlation with Fe-based BMGs [53], however, in contrast to Al-based glasses, which exhibit a monotonically decreasing exothermic DSC signal with no clearly defined exothermic peaks [54]. The length of the incubation time (t_0) as well as the peak positions (t_{peak}) strongly varies with T_{iso} , i.e., the peak maximum occurs at shorter times at higher annealing temperature. The corresponding data are presented in Table 1. From the slope of the $\ln(t_{\text{peak}})$ versus T_{iso}^{-1} function (see Fig. 2b) the isothermal apparent activation energy can be determined [53] and found to be $E_{a,\text{iso}} = 345 \text{ kJ mol}^{-1}$. The similar value obtained for the first crystallization event ($E_{a,x1}$) from the linear heating experiment indicates that the atoms incorporating in the nucleation during both isothermal and non-isothermal treatments acquire, on average, rather similar amount of energy to join an activated cluster. At the

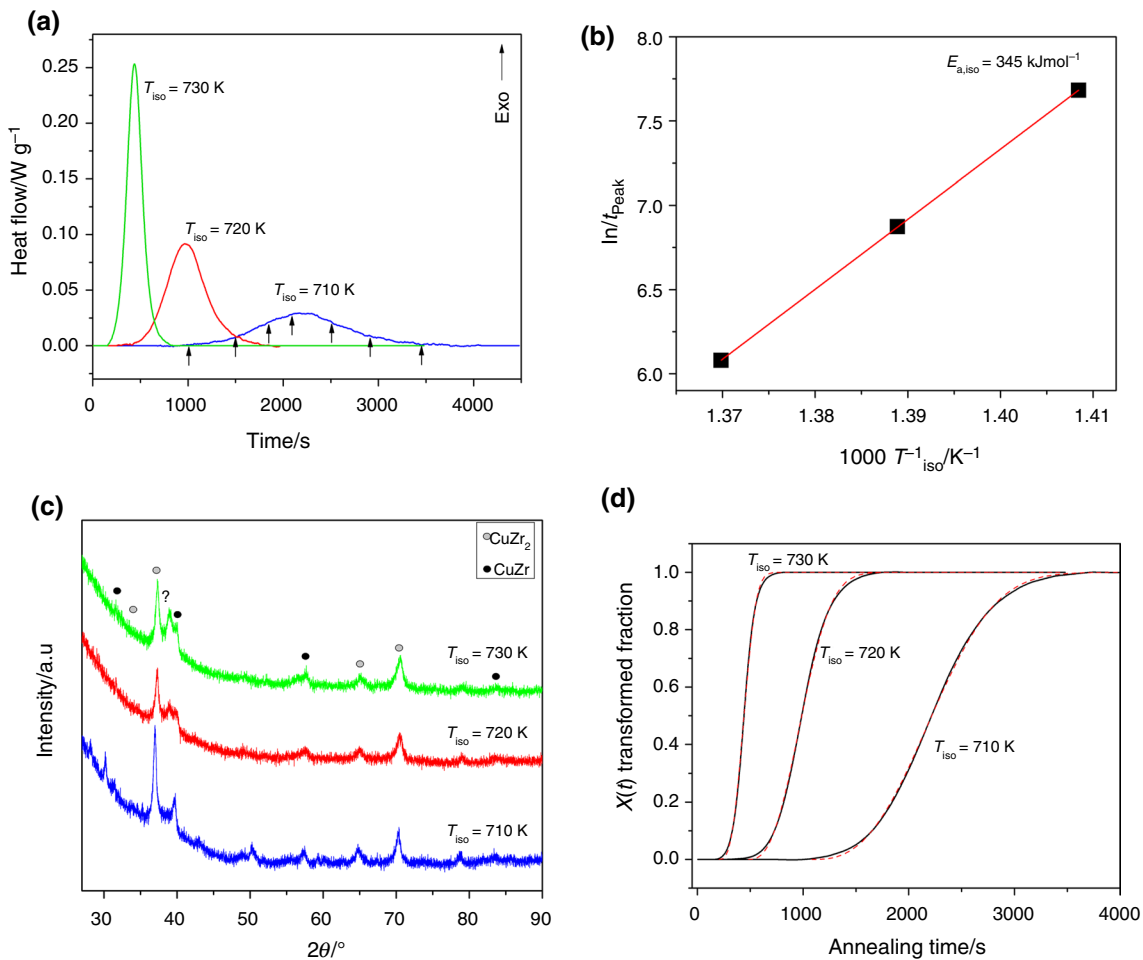


Fig. 2 **a** Isothermal DSC curves of the amorphous $\text{Cu}_{38}\text{Zr}_{54}\text{Al}_8$ glass obtained at different T_{iso} annealing temperatures. The arrows indicate the length of t_{iso} pre-anneals obtained at an isothermal temperature of $T_{\text{iso}} = 710$ K. **b** Logarithm of the isothermal peak positions (t_{peak}) as a function of the inverse of T_{iso} . **c** XRD patterns corresponding to the

isothermally annealed samples obtained at various T_{iso} temperatures. **d** Transformed volume fraction curves of the first crystallization process obtained at different T_{iso} annealing temperatures. Dashed lines are the fitted Avrami functions

Table 1 Characteristic values corresponding to the isothermal treatments of the $\text{Cu}_{38}\text{Zr}_{54}\text{Al}_8$ BMG obtained at different T_{iso} annealing temperatures

T_{iso}/K	t_0/s	t_{peak}/s	$\Delta H_{\text{iso}}/\text{Jg}^{-1}$	Crystalline size/nm	n
710	1300	2203	33	CuZr_2	25
				CuZr	11
720	578	969	47	CuZr_2	21
				CuZr	6
730	267	437	53	CuZr_2	19
				CuZr	6

t_0 denotes the incubation time, t_{peak} is the time corresponds to the maximum of exothermic transformation, ΔH_{iso} is the isothermal heat release and n is the Avrami exponent

same time, the ΔH_{iso} isothermal heat release values for all T_{iso} annealing temperatures (see Table 1) are remarkably lower than the first crystallization transformation obtained during the non-isothermal experiment (ΔH_1), indicating that this event is not completed.

The structure of the isothermally annealed states of the $\text{Cu}_{38}\text{Zr}_{54}\text{Al}_8$ BMG was also examined by XRD. As confirmed by Fig. 2c, the patterns recorded after isothermal annealing exhibits the presence of the same crystalline phases, i.e., CuZr_2 and CuZr as were obtained after

a continuous heating above the first crystallization event ($T_{\text{lin}} = 810$ K), see also Fig. 1a. Similar results have been obtained recently for a $\text{Cu}_{47.5}\text{Zr}_{45.1}\text{Al}_{7.4}$ BMG [55]. The mean crystallite size of these two phases obtained after isothermal annealing shows some variation with T_{iso} , i.e., lower annealing temperature yields the formation of slightly larger nanocrystals, see Table 1. In spite of the similar devitrification products obtained after linear heating above the first crystallization peak ($T_{\text{lin1}} = 810$ K) and after isothermal annealings at $T_{\text{iso}} = 710$ – 730 K, the different enthalpy release may correspond to the different average size of the crystallite products and to the different time scale of the two processes.

It was shown that the change of the total heat release per unit mass, ΔH during a grain-growth process from d_1 to d_2 average crystallite size can be given as

$$\Delta H = \frac{6}{\rho} \gamma_{\text{GB}} \left(\frac{1}{d_1} - \frac{1}{d_2} \right) \quad (3)$$

where ρ is the sample density and γ_{GB} is the average specific grain boundary surface energy [56]. It is assumed in this simple calculation that the grain boundary structure and the associated specific grain boundary energy do not change significantly due to the lack of any phase transformation. In addition, a “virtual” heat release can be introduced between two partial amorphous states containing different volume fraction of the same crystalline phase, which is equal to the measured ΔH_{iso} enthalpy difference between the two states and afterward γ_{GB} can be determined [57]. According to Table 1, the difference in the total enthalpy release between the states obtained by isothermal annealing at $T_{\text{iso}} = 710$ K and $T_{\text{iso}} = 730$ K is 20 Jg^{-1} . With the available average crystallite size values for the CuZr_2 phase γ_{GB} was found to be $1.8 \pm 0.2 \text{ Jm}^{-2}$. This value exceeds that of high angle grain boundaries and might correspond a considerable atomic mismatch generated between the surface atoms of the CuZr_2 nanocrystals and the surrounding amorphous matrix.

In general, the crystallization kinetics of a BMG can be studied by isothermal annealing experiments carried out at temperatures below the linear heating transformation temperature [56]. The transformed volume fraction corresponding to a single exothermic reaction can be evaluated directly from the recorded isothermal heat flow signal after baseline correction (see also Fig. 2a) according to the following equation

$$x(t) = \frac{\int_0^t \Delta \dot{H}_{\text{iso}}(t) dt}{\Delta H_{\text{iso}}}, \quad (4)$$

where $x(t)$ and $\Delta \dot{H}_{\text{iso}}(t)$ are the actual crystallized volume fraction and the recorded heatflow signal at time t , respectively [53]. Figure 2d shows the transformed fraction curves (solid line) obtained from the isothermal annealing experiments by Eq. (4). It is evident from the figure that

the isothermal transformation is completed in shorter times with increasing the annealing temperature. According to the classical Johnson–Mehl–Avrami nucleation theory, $x(t)$ of an isothermal process can be describes as

$$x(t) = 1 - \exp \left[-K(T)(t - t_0)^n \right] \quad (5)$$

where $K(T)$ is a temperature dependent kinetic constant, t_0 is the incubation time and n is the Avrami exponent which varies between 0.5 and 4 depending on the nature of the nucleation and growth mechanism [58]. As seen, the fitted Avrami functions (dashed lines) well follow the $x(t)$ transformation curves in a wide time interval at all T_{iso} temperatures, which assumes that n is constant during almost the whole reaction, while only marginal deviations can be observed at the start and end of the process. As listed in Table 1, the Avrami exponent for $T_{\text{iso}} = 730$ K ($n = 3.0$) corresponds to a diffusion controlled homogeneous nucleation at a constant growth rate of the CuZr_2 and CuZr nanocrystals from the amorphous matrix [59]. The slightly lower n values ($n = 2.6$ – 2.7) for the lower T_{iso} temperatures refer to a slightly decreasing nucleation rate.

Devitrification during partial isotherms

The gradual formation of the microstructure during isothermal annealing was also followed by X-ray diffraction. Figure 3a presents a series of XRD patterns obtained after various t_{iso} pre-annealing times (indicated by arrows in Fig. 2a) carried out at $T_{\text{iso}} = 710$ K. As one can notice, the first crystalline Bragg-peaks appear after $t_{\text{iso}} = 1500$ s of annealing, in coincidence with the t_0 incubation time determined from the isothermal DSC-experiments (see Table 1). As the t_{iso} annealing time increases, the crystalline peaks become more pronounced and, at the same time, the amorphous component vanishes. These patterns confirm the gradual formation of the CuZr and CuZr_2 nanocrystals from the residual amorphous matrix. Figure 3b presents the evolution of the average crystallite size of the major CuZr_2 phase as a function of the isothermal annealing time at $T_{\text{iso}} = 710$ K. The mean size grows throughout the overall crystallization process reaching 23 nm, according to a power law. In the case of normal isothermal grain growth, the variation of grain size can be described as [60]:

$$d^p - d_0^p = K(T)t \quad (6)$$

where d_0 and d represent the initial and the final mean crystallite size values, respectively, $K(T)$ is a temperature dependent rate constant and p is the growth exponent. According to the ideal classical growth theory p is assumed to be 2 [60], however, several factors such as grain boundary segregation, surface impurities and second phase drag

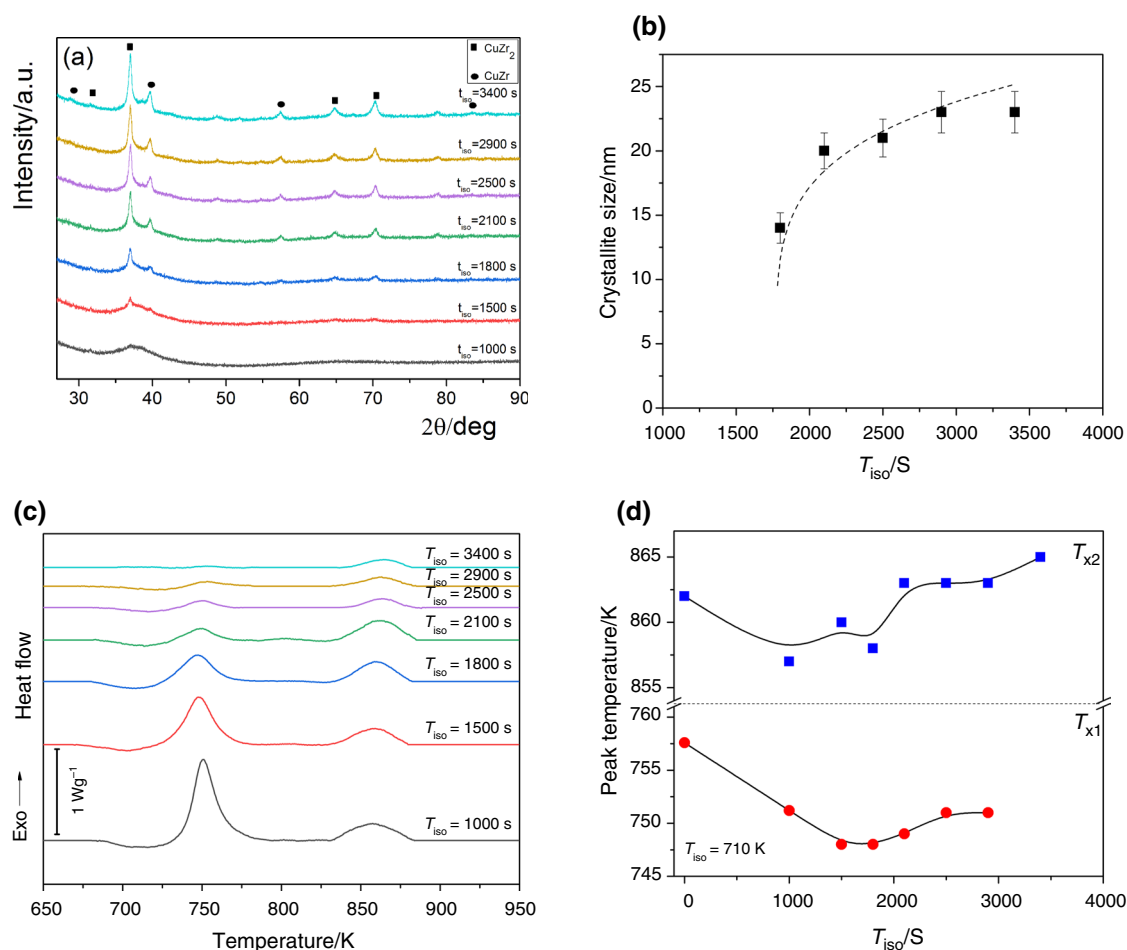


Fig. 3 **a** XRD patterns of samples obtained after different t_{iso} pre-annealing times at $T_{iso} = 710$ K annealing temperature. **b** Variation of the mean crystallite size of the major CuZr₂ phase as a function of the annealing time at $T_{iso} = 710$ K. The dashed line represents the fitted functions according to Eq. (6). **c** Linear heating DSC-curves

(20 K min⁻¹) obtained after different t_{iso} pre-annealings taken at $T_{iso} = 710$ K. **d** Variation of the T_{x1} and T_{x2} peak temperatures corresponding to different t_{iso} pre-annealings of the as-cast BMG at $T_{iso} = 710$ K

can considerably alter this value. Fitting the obtained values by Eq. (6), one can obtain $p = 5.1$ for the growth of the nanocrystalline CuZr₂ particles. Such a high value of p corresponds to a less intensive growth of the CuZr₂ nanocrystals, which can be explained by the slow and component-dependent diffusion of the Cu and Zr atoms within the amorphous matrix toward the already nucleated embryos.

Figure 3c shows the measured linear heating calorimetric curves of the as-cast Cu₃₈Zr₅₄Al₈ BMG after various t_{iso} pre-annealing times taken at $T_{iso} = 710$ K. As it is noticed, the area of the ΔH_1 first peak gradually diminishes with increasing t_{iso} , in accordance with the simultaneous precipitation of the CuZr and CuZr₂ phases, see also Fig. 3a. At the same time the magnitude of the ΔH_2 second peak remains practically unchanged up to $t_{iso} = 2100$ s and still visible after the full completion of the first transformation ($t_{iso} = 3400$ s). As seen in Fig. 3d, both T_{x1} and T_{x2} vary as a function of the

pre-anneal time. The observed decrease in the first transformation temperature is associated with a reduced supercooled liquid range, which might correspond to a slight compositional modification of the residual amorphous component.

High-pressure torsion

The XRD patterns averages from the surface of the HPT-disks exposed to uniaxial compression ($N = 0$) and varying rotational strains ($N = 0.2$, $N = 1$, and $N = 5$) are summarized in Fig. 4a. Similarly to the as-cast glass, all the deformed samples exhibit the same amorphous halo centered at $2\theta \approx 37$ deg, while only very faint peaks superimpose on the amorphous background for the disks processed up to $N = 1$ and $N = 5$ revolutions. As a consequence, the Cu₃₈Zr₅₄Al₈ glass is extremely stable against deformation induced devitrification and subsequent crystallization, which might

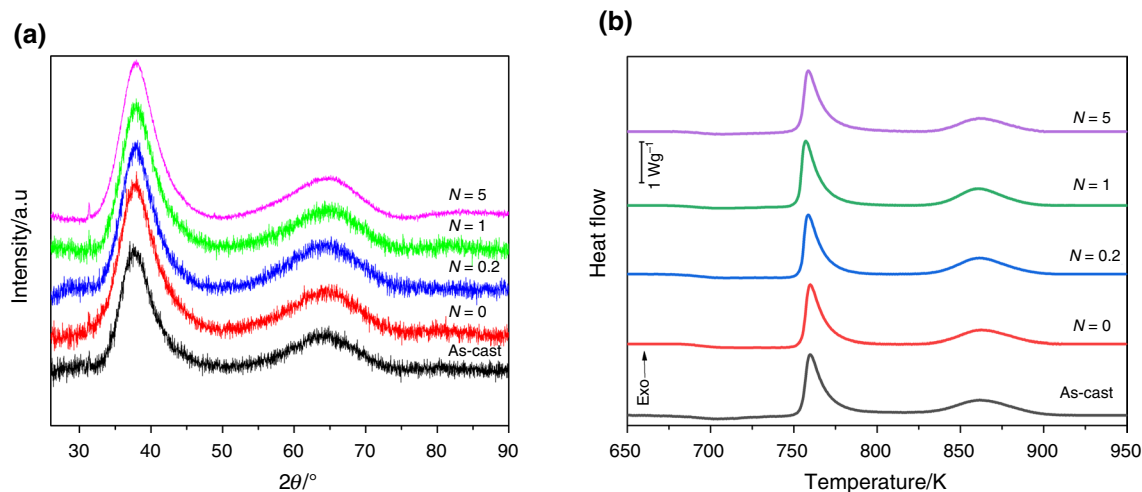


Fig. 4 **a** XRD patterns of the as-cast $\text{Cu}_{38}\text{Zr}_{54}\text{Al}_8$ glass and the HPT-disks processed for different torsion numbers. **b** Continuous-heating DSC curves corresponding to as-cast alloy and different HPT disks

correspond to the presence of Al that can prevent the formation of some crystalline embryos during the casting process and their growth during the shear deformation along enhanced diffusion pathways. As a contrary example, when Ti is added to CuZr, an amorphous $\text{Cu}_{60}\text{Zr}_{20}\text{Ti}_{20}$ BMG suffers a dramatic devitrification and crystallization during the HPT-deformation, since the activation barrier for nucleation is significantly reduced [46].

Apart from its outstanding structural stability, the $\text{Cu}_{38}\text{Zr}_{54}\text{Al}_8$ glass also exhibits extreme thermal stability against the severe shear deformation during HPT, as confirmed by Fig. 4b. It is evident from the figure that the continuous-heating DSC curves corresponding to the deformed states are very similar to that of the as-cast glass, i.e., each curve presents the glass transition and the subsequent T_{x1} and T_{x2} transformations. Similar strong structural and thermal stability of a slightly different composition ($\text{Cu}_{46}\text{Zr}_{46}\text{Al}_8$) against SPD by cold-rolling was confirmed by Eckert and co-workers [61]. As a consequence of the continuous shear, only slight variation in the peak temperatures takes place ($T_{x1} = 758$ K and $T_{x2} = 863$ K), confirming similar thermal stability to the as-cast alloy. At the same time the total heat release (ΔH_{HPT}) varies in the range of 90–99 Jg^{-1} . If it is assumed that the total heat release during linear heating $\Delta H_{\text{tot}} = \Delta H_1 + \Delta H_2$ corresponds only to the amorphous \rightarrow crystalline transformation [62, 63], the $\Delta H_{\text{HPT}}/\Delta H_{\text{tot}}$ ratio should provide the residual amorphous content of the HPT-deformed disks. Accordingly, the severe plastic deformation results in a slight decrease of 77–85% amorphous content, resulting in the nucleation of nanocrystals from the amorphous matrix, in correlation with other high thermal stability metallic glasses [63]. The massive residual amorphous component undoubtedly confirms the exceptional stability of the $\text{Cu}_{38}\text{Zr}_{54}\text{Al}_8$ alloy. In order to

resolve the observed discrepancy between the practically fully amorphous XRD patterns presented in Fig. 4a and the reduced ΔH_{HPT} total heat release, it is assumed that the deformation induced nanocrystals are below (~ 3 – 5 nm) the X-ray resolution limit [64].

Modulated thermal analysis

Modulated calorimetry was first applied in 1993 to explore dynamic thermal characteristics of glassy systems [65], nevertheless metallic glasses have rarely been studied since then [66, 67]. In present study, MDSC was used to separate reversible and irreversible thermal effects in the as-cast and HPT-deformed $\text{Cu}_{38}\text{Zr}_{54}\text{Al}_8$ glassy alloy. The applied heating program (red curve) and the measured heat flow (blue curve) are depicted in Fig. 5a for the as-cast BMG sample. The experimental data were evaluated by fitting a $P(t) = P_0 + t \cdot \beta^* + \Delta P \cdot \sin(2\pi f \cdot t + \varphi)$ function to $1/f$ period long segments of the heat flow data and shifting this fitting segment throughout the full time series, where P_0 and β^* are the actual value and the slope of the heat flow curve, respectively [68, 69]. The resulting $P_0(t)$ average heat flow curve is approximately equivalent to the heat flow signal of the conventional DSC measurements, while $\Delta P(t)$ amplitude and $\varphi(t)$ phase curves characterize the thermal response to the temperature fluctuations of the heating program. This thermal response depends both on the thermal characteristics of the investigated sample and also that of the calorimeter. Reversible heat effect, i.e., heat capacity of the investigated sample is approximately determined by the amplitude, while phase change reports about the irreversible heat effects of the sample [70, 71]. More accurately, the reversible specific heat of the sample was determined as $\text{Re}(c_p) = \Delta P(t) \cdot \cos(\varphi(t) - \varphi_0)$, while the irreversible component of the specific heat was calculated

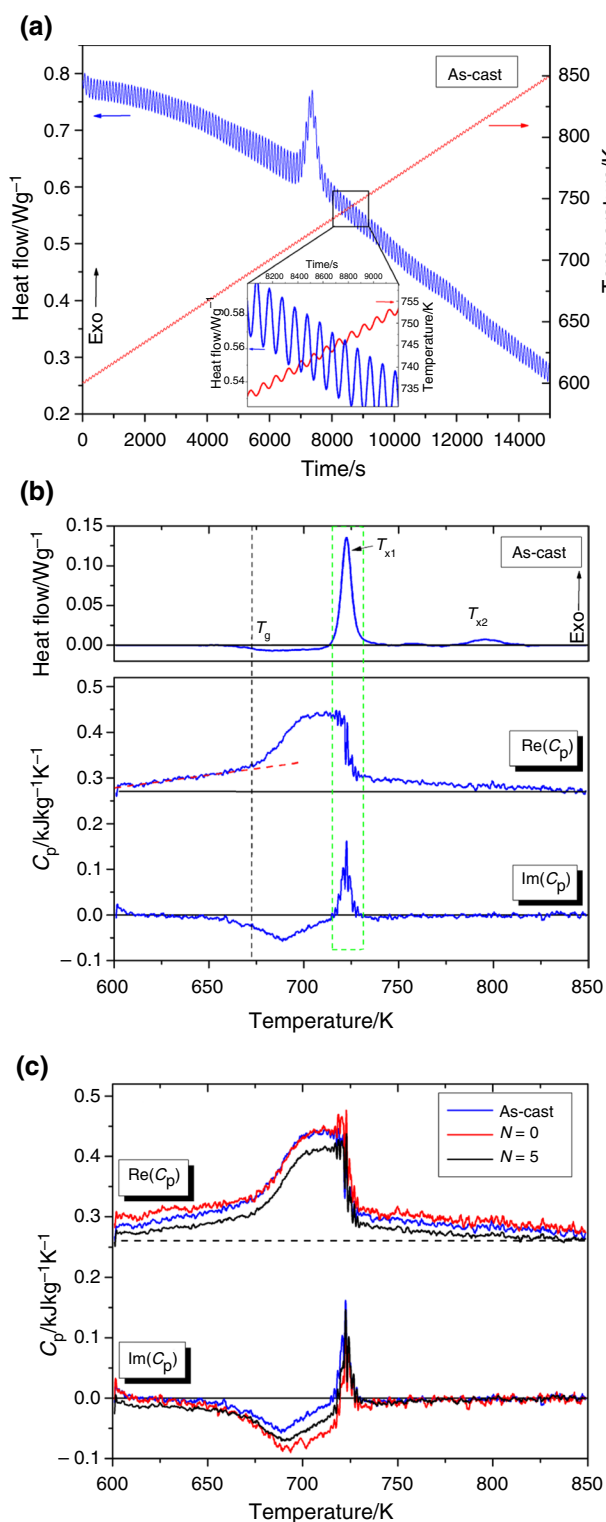


Fig. 5 **a** Temperature vs. time heating program (red curve) of a modulated DSC measurements and the experimental heat flow (blue curve) of the as-cast BMG sample. The inset shows the zoom of the indicated regime of a few periods. **b** Average heat flow curve after the subtraction of the baseline with the reversible and irreversible components of the specific heat of the as-cast BMG sample. **c** Comparison between the specific heat components of the as-cast, $N=0$ and $N=5$ samples

as $Im(c_p) = \Delta P(t) \cdot \sin(\varphi(t) - \varphi_0)$, where φ_0 was determined for each measurement from the average phase of the sample between 825 and 850 K.

Figure 5b shows the average heat flow along with the reversible and irreversible specific heat components between 600 and 850 K for the as-cast BMG sample. Glass transition temperature ($T_g = 672.7$ K), and crystallization peak temperatures ($T_{x1} = 722.5$ K and $T_{x2} = 796.4$ K) can be determined from the average heat flow curve for 1 K min⁻¹ heating rate. In agreement with the increasing atomic mobility in a liquid with respect to its glass state, the reversible specific heat starts to increase rapidly at T_g from $c_p = 0.328$ kJkg⁻¹ K⁻¹ and reaches $c_p = 0.439$ kJkg⁻¹ K⁻¹ in the supercooled liquid region. During this transition the irreversible part of the specific heat shows a negative peak (lambda point) indicating the presence of irreversible heat effects and the relaxation of structural defects during the glass transition. It is noted that the dynamic glass transition determined as the inflection point of the reversible specific heat signal is above T_g obtained from the average heat flow curve, in agreement with Frey et al. [67]. According to that study, the two glass transition temperatures tend to overlap with decreasing f modulation frequency. As seen, below T_g , the as-cast glass already shows a slow change in the glassy state confirmed by the gradual increase in the reversible specific heat and the early of the irreversible negative peak of the specific heat. Similarly, a slow but continuous decrease in the reversible specific heat is present after the first crystallization event which indicates an ongoing slow process between the two crystallization events.

Specific heat curves of the as-cast, compressed ($N=0$) and severe plastic deformed ($N=5$) samples in Fig. 5c show rather similar behavior for all the samples. However, the reversible specific heat of the compressed $N=0$ sample is typically higher, while the same specific heat of the severe plastic deformed sample ($N=5$) is lower than that of the as-cast BMG. These observations indicate the presence of extra defects in the glassy state for the compressed sample and a more ordered (severely sheared) glassy structure for the severe plastic deformed glass in agreement with previous observations on the deformation induced anisotropy of BMGs [34, 72].

Conclusions

Cu₃₈Zr₅₄Al₈ bulk metallic glass exhibits a two-stage crystallization sequence with a combination of excellent GFA parameters ($T_g = 671$ K, $\Delta T_x = 80$ K, $T_r = 0.57$ and $\gamma = 0.41$). The obtained activation energy values corresponding to crystallization ($E_{a,x1} = 325$ kJ mol⁻¹, $E_{a,x2} = 210$ kJ mol⁻¹) confirm the high thermal stability of the glass. Isothermal annealing experiments carried out above T_g reveal a single

exothermic peak and Johnson–Mehl–Avrami kinetics with diffusion-controlled homogeneous nucleation at a constant growth rate. The isothermal growth of nanocrystals follows a power law function with an exponent $p = 5.1$.

The extremely high structural stability of the $\text{Cu}_{38}\text{Zr}_{54}\text{Al}_8$ glass against severe shear deformation by HPT is confirmed by XRD, i.e., the patterns of the deformed disks are characterized by a dominant amorphous halo. Calorimetric studies have indicated that severe plastic deformation results in a slight decrease to 77–85% of the initial amorphous content.

Modulated DSC investigations revealed that the as-cast $\text{Cu}_{38}\text{Zr}_{54}\text{Al}_8$ BMG already shows a slow change in the glassy state below T_g confirmed by the gradual increase in the reversible specific heat. For the compressed sample the reversible specific heat is higher, while for the severe plastic deformed sample it is lower than that of the as-cast sample. These results indicate the presence of extra defects in the compressed state, while a more ordered glassy structure for the severely sheared deformed state.

Acknowledgements T. A. is indebted for the Hungarian Tempus organization for providing a Stipendium Hungaricum Ph.D. scholarship.

Author contributions ÁR: Calorimetry and X-ray diffraction measurements, high-pressure torsion, writing, editing, reviewing. TA: Calorimetry and X-ray diffraction measurements, writing. ES: high-pressure torsion. DJB: preparation of as-cast glass, reviewing. ZK: modulated calorimetry, editing, reviewing.

Funding Open access funding provided by Eötvös Loránd University.

Declarations

Conflict of interest The authors have no conflict of interest to declare that are relevant to the content of this article.

Open Access This article is licensed under a Creative Commons Attribution 4.0 International License, which permits use, sharing, adaptation, distribution and reproduction in any medium or format, as long as you give appropriate credit to the original author(s) and the source, provide a link to the Creative Commons licence, and indicate if changes were made. The images or other third party material in this article are included in the article's Creative Commons licence, unless indicated otherwise in a credit line to the material. If material is not included in the article's Creative Commons licence and your intended use is not permitted by statutory regulation or exceeds the permitted use, you will need to obtain permission directly from the copyright holder. To view a copy of this licence, visit <http://creativecommons.org/licenses/by/4.0/>.

References

- Inoue A. Stabilization of metallic supercooled liquid and bulk amorphous alloys. *Acta Mater.* 2000;48:279–306. [https://doi.org/10.1016/S1359-6454\(99\)00300-6](https://doi.org/10.1016/S1359-6454(99)00300-6).
- Zhang Y, Wang WH, Greer AL. Making metallic glasses plastic by control of residual stress. *Nat Mater.* 2006;5:857–60. <https://doi.org/10.1038/nmat1758>.
- Trexler MM, Thadhani NN. Mechanical properties of bulk metallic glasses. *Prog Mater Sci.* 2010;55:759–839. <https://doi.org/10.1016/j.pmatsci.2010.04.002>.
- Greer AL, Ma E. Bulk metallic glasses: at the cutting edge of metals research. *MRS Bull.* 2007;32:611–9. <https://doi.org/10.1557/mrs2007.121>.
- Yavari AR, Lewandowski JJ, Eckert J. Mechanical properties of bulk metallic glasses. *MRS Bull.* 2007;32:635–8. <https://doi.org/10.1557/mrs2007.125>.
- Miller M, Liaw P. Bulk metallic glasses. New York: Springer; 2008. <https://doi.org/10.1007/978-0-387-48921-6>.
- Cheng YQ, Ma E. Atomic-level structure and structure–property relationship in metallic glasses. *Prog Mater Sci.* 2011;56:379–473. <https://doi.org/10.1016/j.pmatsci.2010.12.002>.
- Miracle DB, Egami T, Floresa KM, Kelton KF. Structural aspects of metallic glasses. *MRS Bull.* 2007;32:629–34. <https://doi.org/10.1557/mrs2007.124>.
- Schuh CA, Hufnagel TC, Ramamurty U. Mechanical behavior of amorphous alloys. *Acta Mater.* 2007;55:4067–109. <https://doi.org/10.1016/j.actamat.2007.01.052>.
- Miracle DB. The efficient cluster packing model—an atomic structural model for metallic glasses. *Acta Mater.* 2006;54:4317–36. <https://doi.org/10.1016/j.actamat.2006.06.002>.
- Egami T, Vitek V. Local structural fluctuations and defects in metallic glasses. *J Non-Cryst Solids.* 1984;61–62:499–510. [https://doi.org/10.1016/0022-3093\(84\)90596-9](https://doi.org/10.1016/0022-3093(84)90596-9).
- Cai AH, Feng YJ, Ding DW, Liu Y, Wu H, An Q, Ning H, Zhou GJ, Peng YY. Effect of Fe–C alloy additions on properties of Cu–Zr–Ti metallic glasses. *J Alloys Comp.* 2019;798:273–9. <https://doi.org/10.1016/j.jallcom.2019.05.256>.
- Révész Á, Concustell A, Varga LK, Suriñach S, Baró MD. Influence of the wheel speed on the thermal behaviour of $\text{Cu}_{60}\text{Zr}_{20}\text{Ti}_{20}$ alloys. *Mater Sci Eng A.* 2004;375–377:776–80. <https://doi.org/10.1016/j.msea.2003.10.151>.
- Yu P, Bai HY, Wang WH. Superior glass-forming ability of CuZr alloys from minor additions. *J Mater Res.* 2006;21:1674–9. <https://doi.org/10.1557/jmr.2006.0212>.
- Feng Y, Cai AH, Ding DW, Liu Y, Wu H, An Q, Ning H, Zhou GJ, Peng YY. Composition design and properties of Cu–Zr–Ti bulk metallic glass composites. *Mater Chem Phys.* 2019;232:452–9. <https://doi.org/10.1016/j.matchemphys.2019.05.030>.
- Inoue A, Nishiyama N. New bulk metallic glasses for applications as magnetic-sensing, chemical and structural materials. *MRS Bull.* 2007;32:651–8. <https://doi.org/10.1557/mrs2007.128>.
- Concustell A, Zielinska M, Révész Á, Varga LK, Suriñach S, Baró MD. Thermal characterization of $\text{Cu}_{60}\text{Zr}_x\text{Ti}_{40-x}$ metallic glasses ($x=15, 20, 22, 25, 30$). *Intermetallics.* 2004;12:1063–7. <https://doi.org/10.1016/j.intermet.2004.04.023>.
- Xu D, Lohwongwatan B, Duan G, Johnson WL, Garland C. Bulk metallic glass formation in binary Cu-rich alloy series— $\text{Cu}_{100-x}\text{Zr}_x$ ($x=34, 36, 38.2, 40$ at.%) and mechanical properties of bulk $\text{Cu}_{64}\text{Zr}_{36}$ glass. *Acta Mater.* 2004;52:2621–4. <https://doi.org/10.1016/j.actamat.2004.02.009>.
- Lee JC, Park KW, Kim KH, Fleury E, Lee BJ, Wakeda M, Shibutani Y. Origin of the plasticity in bulk amorphous alloys. *J Mater Res.* 2007;22:3087–97. <https://doi.org/10.1557/JMR.2007.0382>.
- Pan Y, Zeng Y, Jing L, Zhang L, Pi J. Composition design and mechanical properties of ternary Cu–Zr–Ti bulk metallic glasses. *Mater Design.* 2014;55:773–7. <https://doi.org/10.1016/j.matdes.2013.10.057>.
- Sarac B. Influence of sub-glass transition heat-treatment on physical and structural properties of $\text{Cu}_{46}\text{Zr}_{44}\text{Al}_8\text{Hf}_2$ metallic glass. *Res Eng Struct Mat.* 2021;7:121–34. <https://doi.org/10.17515/resm2020.205ma0811>.
- Cui X, Zhang XF, Li JJ, Zu FQ, Meng LZ, Lu J, Luo F, Ma YB. Centimeter-sized CuZrAl bulk metallic glass with good plasticity

- and chemical heterogeneity. *Intermetallics*. 2020;121: 106773. <https://doi.org/10.1016/j.intermet.2020.106773>.
23. Xu Y, Jeurgens LPH, Bo H, Lin L, Zhu S, Huang Y, Liu Y, Qiao J, Wang Z. On the competition between synchronous oxidation and preferential oxidation in Cu–Zr–Al metallic glasses. *Corros Sci*. 2020;177: 108996. <https://doi.org/10.1016/j.corsci.2020.108996>.
 24. Wang Q, Qiang J, Wang Y, Xia J, Dong C. Bulk metallic glass formation in Cu–Zr–Ti ternary system. *J Non-Cryst Solids*. 2007;353:3425–8. <https://doi.org/10.1016/j.jnoncrysol.2007.05.093>.
 25. Luo Y, Jiang Y, Zhang P, Wang X, Ke H, Zhang P. A novel Ni-free Zr-based bulk metallic glass with high glass forming ability. Corrosion resistance and thermal stability. *Chin J Mech Eng*. 2020;33:65. <https://doi.org/10.1186/s10033-020-00482-y>.
 26. Pauly S, Bednarcik J, Kühn U, Eckert J. Plastically deformable Cu–Zr. *Intermet Scr Mater*. 2010;63:336–8. <https://doi.org/10.1016/j.scriptamat.2010.04.034>.
 27. Pauly S, Gorantla S, Wang G, Kühn U, Eckert J. Transformation-mediated ductility in CuZr-based bulk metallic glasses. *Nat Mater*. 2010;9:473–7. <https://doi.org/10.1038/nmat2767>.
 28. Song K, Wu S, Kaban I, Stoica M, Bednarcik J, Sun B, Cao C, Wang G, Wang L, Eckert J. In situ high-energy X-ray diffraction study of thermally-activated martensitic transformation far below room temperature in CuZr-based bulk metallic glass composites. *J Alloy Compd*. 2020;841: 155781. <https://doi.org/10.1016/j.jallcom.2020.155781>.
 29. Lu X, Nursulton M, Du Y, Liao W. Structural and mechanical characteristics of $\text{Cu}_{50}\text{Zr}_{43}\text{Al}_{7}$ bulk metallic glass fabricated by selective laser melting. *Materials*. 2019;12:775. <https://doi.org/10.3390/ma12050775>.
 30. Chen Y, Liang W, Wang L, Qi K, Wang Y, Sun X, Fang N. Effect of sample-size on the compression deformation behavior of a CuZr-based bulk metallic glass composite. *Metals*. 2020;10(7):857. <https://doi.org/10.3390/met10070857>.
 31. Sort J, Ile DC, Zhilyaev AP, Concustell A, Czepe T, Stoica M, Suriñach S, Eckert J, Baró MD. Cold-consolidation of ball-milled Fe-based amorphous ribbons by high pressure torsion. *Scr Mater*. 2004;50:1221–5. <https://doi.org/10.1016/j.scriptamat.2004.02.004>.
 32. Edalati K, Fujita I, Sauvage X, Arita M, Horita Z. Microstructure and phase transformations of silica glass and vanadium oxide by severe plastic deformation via high-pressure torsion straining. *J Alloys Compd*. 2019;779:394–8. <https://doi.org/10.1016/j.jallcom.2018.11.086>.
 33. Kovács ZS, Henits P, Zhilyaev AP, Révész Á. Deformation induced primary crystallization in a thermally non-primary crystallizing amorphous $\text{Al}_{85}\text{Ce}_8\text{Ni}_5\text{Co}_2$ alloy. *Scr Mater*. 2006;54:1733–7. <https://doi.org/10.1016/j.scriptamat.2006.02.004>.
 34. Révész Á, Schaffler E, Kovács ZS. Structural anisotropy in a $\text{Zr}_{57}\text{Ti}_5\text{Cu}_{20}\text{Al}_{10}\text{Ni}_8$ bulk metallic glass deformed by high pressure torsion at room temperature. *Appl Phys Lett*. 2008;92:011910. <https://doi.org/10.1063/1.2830992>.
 35. Valiev RZ, Ishlamgaliev RK, Alexandrov IV. Bulk nanostructured materials from severe plastic deformation. *Prog Mater Sci*. 2000;45:103–89. [https://doi.org/10.1016/S0079-6425\(99\)00007-9](https://doi.org/10.1016/S0079-6425(99)00007-9).
 36. Edalati K, Horita Z. A review on high-pressure torsion (HPT) from 1935 to 1988. *Mater Sci Eng A*. 2016;652:325–52. <https://doi.org/10.1016/j.msea.2015.11.074>.
 37. Zhilyaev AP, Langdon TG. Using high-pressure torsion for metal processing: fundamentals and applications. *Prog Mater Sci*. 2008;53:893–979. <https://doi.org/10.1016/j.pmatsci.2008.03.002>.
 38. Rezvani A, Sarac B, Soprunyuk V, Kim JT, Song KK, Li CJ, Schranz W, Eckert J. Influence of combinatorial annealing and plastic deformation treatments on the intrinsic properties of $\text{Cu}_{46}\text{Zr}_{46}\text{Al}_8$ bulk metallic glass. *Intermetallics*. 2020;127: 106986. <https://doi.org/10.1016/j.intermet.2020.106986>.
 39. Hóbor S, Révész Á, Szabó PJ, Zhilyaev AP, Kovács Kis V, Lábár JL, Kovács ZS. High pressure torsion of amorphous $\text{Cu}_{60}\text{Zr}_{30}\text{Ti}_{10}$ alloy. *J Appl Phys*. 2008;104:033525. <https://doi.org/10.1063/1.2964115>.
 40. Hóbor S, Kovács ZS, Révész Á. Macroscopic thermoplastic model applied to the high pressure torsion of metallic glasses. *J Appl Phys*. 2009;109:023531. <https://doi.org/10.1063/1.3176950>.
 41. Hóbor S, Kovács ZS, Zhilyaev AP, Varga LK, Szabó PJ, Révész Á. High pressure torsion of Cu-based metallic glasses. *J Phys Conf Series*. 2010;240:012153. <https://doi.org/10.1088/1742-6596/240/1/012153>.
 42. Hóbor S, Kovács ZS, Révész Á. Effect of accumulated shear on the microstructure and morphology of severely deformed $\text{Cu}_{60}\text{Zr}_{30}\text{Ti}_{10}$ metallic glass. *J All Comp*. 2011;509:8641–8. <https://doi.org/10.1016/j.jallcom.2011.06.046>.
 43. Malekan M, Rashidi R. Effective role of minor silicon addition on crystallization kinetics of $\text{Cu}_{50}\text{Zr}_{43}\text{Al}_7$ bulk metallic glass. *Appl Phys A*. 2021. <https://doi.org/10.1007/s00339-021-04394-z>.
 44. Cao G, Liu K, Liu G, Zong H, Bala H, Zhang B. Improving the glass-forming ability and the plasticity of Zr-Cu-Al bulk metallic glass by addition of Nb. *J Non-Cryst Solids*. 2019;513:105–10. <https://doi.org/10.1016/j.jnoncrysol.2019.03.009>.
 45. Rashidia R, Malekana M, Gholamipour R. Crystallization kinetics of $\text{Cu}_{47}\text{Zr}_{47}\text{Al}_6$ and $(\text{Cu}_{47}\text{Zr}_{47}\text{Al}_6)_{99}\text{Sn}_1$ bulk metallic glasses. *J Non-Cryst Solids*. 2018;498:272–80. <https://doi.org/10.1016/j.jnoncrysol.2018.06.042>.
 46. Révész Á, Horváth A, Ribárik G, Schaffler E, Browne DJ, Kovács Z. Crystallization of $\text{Cu}_{60}\text{Zr}_{20}\text{Ti}_{20}$ bulk metallic glass by high pressure torsion. *Rev Adv Mater Sci*. 2019;58:304–12. <https://doi.org/10.1515/rams-2019-0037>.
 47. Malekan M, Rashidi R, Shabestari SG. Mechanical properties and crystallization kinetics of Er-containing Cu–Zr–Al bulk metallic glasses with excellent glass forming ability. *Vacuum*. 2020;174: 109223. <https://doi.org/10.1016/j.vacuum.2020.109223>.
 48. Lu ZP, Liu CT. A new glass-forming ability criterion for bulk metallic glasses. *Acta Mater*. 2003;50:3501–12. [https://doi.org/10.1016/S1359-6454\(02\)00166-0](https://doi.org/10.1016/S1359-6454(02)00166-0).
 49. Klug HP, Alexander LE. X-ray diffraction procedures: for polycrystalline and amorphous materials. New York: John Wiley & Sons; 1974. <https://doi.org/10.1002/bbpc.19750790622>.
 50. Kissinger HE. Reaction kinetics in differential thermal analysis. *Anal Chem*. 1957;29:1702–6. <https://doi.org/10.1021/ac60131a045>.
 51. Inoue A, Nakazato K, Kawamura Y, Tsai AP, Masumoto T. Effect of Cu or Ag on the formation of coexistent nanoscale Al particles in Al–Ni–M–Ce (M=Cu or Ag) amorphous alloys. *Mater Trans JIM*. 1994;35:95–102. <https://doi.org/10.2320/matertrans1989.35.95>.
 52. Chen LC, Spaepen F. Calorimetric evidence for the micro-quasicrystalline structure of “amorphous” Al transition metal alloys. *Nature*. 1988;336:366–8. <https://doi.org/10.1038/336366a0>.
 53. Révész Á. Crystallization kinetics and thermal stability of an amorphous $\text{Fe}_{77}\text{C}_3\text{B}_4\text{Al}_2\text{GaP}_0\text{Si}_2$ bulk metallic glass. *J Therm Anal and Calorimetry*. 2008;91:879–84. <https://doi.org/10.1007/s10973-007-8632-4>.
 54. Gich M, Gloriant T, Surinach S, Greer AL, Baró MD. Glass forming ability and crystallisation processes within the Al–Ni–Sm system. *J Non-Cryst Solids*. 2001;289:214–20. [https://doi.org/10.1016/S0022-3093\(01\)00650-0](https://doi.org/10.1016/S0022-3093(01)00650-0).
 55. Jiang HR, Hu JY, Neuber N, Bochtler B, Adam B, Riegler SS, Frey M, Ruschel L, Lu WF, Feng AH, Busch R, Shen J. Effect of sulfur on the glass-forming ability, phase transformation, and

- thermal stability of Cu–Zr–Al bulk metallic glass. *Acta Mater.* 2021;212: 116923. <https://doi.org/10.1016/j.actamat.2021.116923>.
56. Révész Á, Varga LK, Surinach S, Baró MD. Thermal stability, crystallization kinetics, and grain growth in an amorphous $\text{Al}_{35}\text{Ce}_5\text{Ni}_8\text{Co}_2$ alloy. *J Mater Res.* 2002;17:2140–6. <https://doi.org/10.1557/JMR.2002.0315>.
57. Révész Á, Lendvai J, Cziráki Á, Liebermann HH, Bakonyi I. Formation of nanocrystalline phases during thermal decomposition of amorphous Ni–P alloys by isothermal annealing. *J Nanosci Nanotech.* 2001;1:191–200. <https://doi.org/10.1166/jnn.2001.020>.
58. Avrami M. Granulation, phase change, and microstructure kinetics of phase change. III. *J Chem Phys.* 1941;9:177. <https://doi.org/10.1063/1.1750872>.
59. Christian JW. The theory of transformations in metals and alloys: an advanced textbook in physical metallurgy. Oxford: Pergamon Press; 1975.
60. Atkinson HV. Overview no. 65: theories of normal grain growth in pure single phase systems. *Acta Metall.* 1988;36:469–91. [https://doi.org/10.1016/0001-6160\(88\)90079-X](https://doi.org/10.1016/0001-6160(88)90079-X).
61. Ma GZ, Song KK, Sun BA, Yan ZJ, Kühn U, Chen D, Eckert J. Effect of cold-rolling on the crystallization behavior of a CuZr-based bulk metallic glass. *J Mater Sci.* 2013;48:6825–32. <https://doi.org/10.1007/s10853-013-7488-1>.
62. Jiang JZ, Kato H, Ohsuna T, Saida J, Inoue A, Saksl K, Franz H, Stahl K. Origin of nondetectable x-ray diffraction peaks in nanocomposite CuTiZr alloys. *App Phys Lett.* 2003;83:3299. <https://doi.org/10.1063/1.1619220>.
63. Révész Á, Kis-Tóth Á, Varga LK, Schafner E, Bakonyi I, Spassov T. Hydrogen storage of melt-spun amorphous $\text{Mg}_{65}\text{Ni}_{20}\text{Cu}_5\text{Y}_{10}$ alloy deformed by high-pressure torsion. *Int J Hydrog Energy.* 2012;37:5769–76. <https://doi.org/10.1016/j.ijhydene.2011.12.160>.
64. Révész Á, Kovács Z. Severe plastic deformation of amorphous alloys. *Mater Trans.* 2019;60:1283–93. <https://doi.org/10.2320/matertrans.MF201917>.
65. Reading M, Elliott D, Hill VL. A new approach to the calorimetric investigation of physical and chemical transitions. *J Therm Anal.* 1993;40:949–55. <https://doi.org/10.1007/BF02546854>.
66. Qiao J, Casalini R, Pelletier JM, Kato H. Characteristics of the structural and Johari-Goldstein relaxations in Pd-based metallic glass-forming liquids. *J Phys Chem B.* 2014;118:3720–30. <https://doi.org/10.1021/jp4121782>.
67. Frey M, Neuber N, Gross O, Zimmer B, Possart W, Busch R. Determining the fragility of bulk metallic glass forming liquids via modulated DSC. *J Phys Condens Matter.* 2020;32:324004. <https://doi.org/10.1088/1361-648X/ab8526>.
68. Jiang Z, Imrie CT, Hutchinson JM. An introduction to temperature modulated differential scanning calorimetry (TMDSC): a relatively non-mathematical approach. *Thermochim Acta.* 2002;387:75–93. [https://doi.org/10.1016/S0040-6031\(01\)00829-2](https://doi.org/10.1016/S0040-6031(01)00829-2).
69. Carpentier L, Bustin O, Descamps M. Temperature-modulated differential scanning calorimetry as a specific heat spectroscopy. *J Phys D Appl Phys.* 2002;35:402–8.
70. Schawe JEK, Höhne GWH. Modulated temperature DSC measurements relating to the cold crystallization process of poly (ethylene terephthalate). *J Thermal Anal.* 1996;46:893–903. <https://doi.org/10.1007/bf01983609>.
71. Schawe JEK. Principles for the interpretation of modulated temperature DSC measurements. Part 1. Glass transition. *Thermochim Acta.* 1995;261:183–94. [https://doi.org/10.1016/0040-6031\(95\)02315-S](https://doi.org/10.1016/0040-6031(95)02315-S).
72. Révész Á, Henits P, Kovács Z. Structural changes in Zr-based bulk metallic glasses deformed by high pressure torsion. *J Alloys Compds.* 2010;495:338–40. <https://doi.org/10.1016/j.jallcom.2009.10.175>.

Publisher's Note Springer Nature remains neutral with regard to jurisdictional claims in published maps and institutional affiliations.